

Pore network modeling of the effects of viscosity ratio and pressure gradient on steady-state incompressible two-phase flow in porous media

Magnus Aa. Gjennestad^{a,*}, Mathias Winkler^a, Alex Hansen^a

^a*PoreLab and Department of Physics, Norwegian University of Science and Technology, Trondheim, Norway*

Abstract

We perform more than 6000 steady-state simulations with a dynamic pore network model, corresponding to a large span in viscosity ratios and capillary numbers. From these simulations, dimensionless quantities such as relative permeabilities, residual saturations, mobility ratios and fractional flows are computed. Relative permeabilities and residual saturations show many of the same qualitative features observed in other experimental and modeling studies. However, while other studies find that relative permeabilities converge to straight lines at high capillary numbers we find that this is not the case when viscosity ratios are different from 1. Our conclusion is that departure from straight lines occurs when fluids mix rather than form decoupled flow channels. Another consequence of the mixing is that computed fractional flow curves, plotted against saturation, lie closer to the diagonal than they would otherwise do. At lower capillary numbers, fractional flow curves have a classical S-shape. Ratios of average mobility to their high-capillary number limit values are also considered. These vary, roughly, between 0 and 1, although values larger than 1 are also observed. For a given saturation and viscosity ratio, the mobilities are not always monotonically increasing with the pressure gradient. While increasing the pressure gradient mobilizes more fluid and activates more flow paths, when the mobilized fluid is more viscous, a reduction in average mobility may occur.

Keywords: porous media, two-phase flow, steady-state, pore network model

1. Introduction

A number of different modeling approaches have been applied to study two-phase flow in porous media. These include direct numerical simulations (DNS), which employ e.g. the volume-of-fluid method [1] or the level-set method [2, 3]

*Corresponding author.

Email address: magnus@aaashammer.net (Magnus Aa. Gjennestad)

to keep track of the fluid interfaces, lattice-Boltzmann methods [4] and pore network models. Recently, a number of methods were compared in a benchmark study by Zhao et al. [5], where participants were asked to reproduce experimentally studied transient fluid displacement processes at different capillary numbers and wettability conditions, i.e. contact angles. The conclusion was that no single method was successful under all conditions and that thin films and corner flow posed substantial computational and modeling challenges.

This benchmark study, and the bulk of works in the literature, focus on transient processes. Less attention has been given to pore-scale modeling and experiments in steady-state flow, i.e. flow where macroscopic quantities such as fractional flow fluctuate around a well-defined mean. On the modeling side, part of the explanation is probably that steady-state simulations require large systems and longer simulation times compared to transient processes. While break-through of the invading phase typically happens for simulation times corresponding to much less than one pore volume of flow in transient cases, several pore volumes may be required to obtain decent time-averages of steady-state quantities.

In spite of this, some studies on steady-state two-phase flow have been done. Avraam and Payatakes [6] did quasi-2D micro model experiments, varied the capillary number, the viscosity ratio and the flow rate ratio, and found four different flow regimes. They also studied relative permeabilities. Steady-state simulations with a pore network model of the Aker type [7] have also been performed by e.g. Knudsen et al. [8], Knudsen and Hansen [9] and Ramstad and Hansen [10]. In particular, Knudsen et al. [8] did simulations with equal viscosities and one value for the interfacial tension, and studied effect of changing total flow rate on e.g. fractional flow and relative permeabilities. Results for equal viscosities are interesting and applicable in some cases, e.g. for mineral oil and water [11]. In other applications, e.g. sequestration of supercritical CO₂ [12] and gas-liquid flows such as in fuel cells, they are not.

We present results from more than 6000 steady-state simulations, that cover a large range of viscosity ratios and capillary numbers. The chosen pore network model is also of the Aker type [7], specifically the variant described by Gjennestad et al. [13]. Other variants of the Aker model can be found in [8–10, 14]. The model has several properties that are advantageous when computing steady-state quantities. First, it is dynamic and thus captures the effects of both viscous and capillary forces. Second, it can be solved in a numerically stable manner at arbitrarily low capillary numbers [13]. Third, it is possible to apply periodic boundary conditions, keeping the saturation constant and eliminating effects of saturation gradients. Furthermore, it is computationally cheap, making the study of large enough systems over long enough times possible.

In spite of these advantages, however, the model also has some limitations. In particular, film flow is not accounted for and the construction of the model makes it difficult to capture accurately cooperative pore-filling events during imbibition [5]. While film flow effects could, in principle, be captured e.g. by a DNS or lattice-Boltzmann method, very high spatial resolution is required to resolve such films properly [5]. This makes such an approach prohibitively ex-

pensive for steady-state calculations, especially when a large number of them are desired. Film flow could, in principle, also be included in the present model [15]. However, use of this modified model at low capillary numbers would probably require the construction of a new solution method to ensure numerical stability. Cooperative pore filling events were more accurately captured by other models in the benchmark study [5]. However, these relied on quasi-static considerations, making them difficult to apply directly in a steady-state simulation.

In the simulations, we utilize a recent innovation in the numerical solution method [13] to perform numerically stable simulations at low and moderate capillary numbers. The new methodology has an important effect at capillary numbers below 10^{-3} . In addition, we make extensive use of a recent study of the high-capillary number regime [16] in the analysis of the results. The discussion is restricted to capillary numbers above 10^{-4} , where history-dependence of the steady-state quantities is negligible [8]. At lower capillary numbers, steady-state quantities are harder to define and calculate. To allow for a discussion which is as general as possible, and which allows for comparison with other studies of slightly different systems, we focus on dimensionless steady-state quantities, such as relative permeabilities, mobility ratios and fractional flow¹. To aid further research, the simulation data are published along with this article.

The aim is to shed light on how different steady-state flow properties behave as capillary numbers are changed from moderate values around 10^{-3} - 10^{-4} to the high capillary number limit and to assess the impact of viscosity ratio in this context. One important finding is that relative permeabilities are not necessarily straight lines at high capillary numbers. Our conclusion is that this occurs when fluids have different viscosities and exhibit some degree of mixing rather than forming separate flow channels. Another interesting finding is that the average mobility, for a given saturation and viscosity ratio, is not always a monotonically increasing function of the pressure gradient. Intuitively, one might think this should be the case, as increasing the pressure gradient mobilizes more fluid and activates more flow paths. However, when the mobilized fluid is more viscous, a reduction in average mobility may occur instead.

The rest of the paper is structured as follows. In Section 2, we describe the system under consideration and define some important steady-state flow properties. In Section 3, we briefly describe the pore network model used and the numerical methods used to solve it. The performed simulations are described in Section 4. Results are presented and discussed in Section 5 and concluding remarks are given in Section 6.

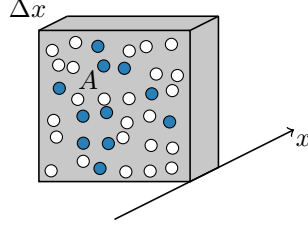


Figure 1: Illustration of the system under consideration, a block of porous material. The porous matrix is shown in gray, pores filled with the wetting fluid in white and pores filled with the non-wetting fluid in blue. The block has thickness Δx in the x -direction and cross sectional area A .

2. System

The system we consider is a block of porous material, as illustrated in Figure 1. It has cross sectional area A and thickness Δx in the direction of flow (the x -direction). The volume of the block is

$$V = A\Delta x. \quad (1)$$

The pore space volume in the block is V_p , so that the porosity is

$$\varphi = V_p/V. \quad (2)$$

The pore space is filled with two fluids, where one is more wetting towards the pore walls than the other. In the following, we will call the more wetting fluid wetting (w) and the less wetting fluid non-wetting (n). The fluids are assumed to be incompressible and S_w is the wetting fluid saturation, i.e. the fraction of the pore space volume occupied by the wetting fluid.

A pressure difference Δp , either constant or fluctuating, exists across the porous block. This causes the wetting and non-wetting fluids to flow at rates Q_w and Q_n , respectively. The total flow rate is,

$$Q = Q_w + Q_n, \quad (3)$$

and the fractional flow of wetting fluid is

$$F_w = Q_w/Q. \quad (4)$$

The average fluid velocity in the pore space, the seepage velocity, is

$$v = Q/\varphi A. \quad (5)$$

¹These quantities are used to provide a familiar framework of dimensionless quantities in which results are presented and discussed. However, other quantities could also, in principle, be used to convey the same information. One example is the velocities presented in [17].

3. Pore network model

In this section, we briefly describe the pore network model used in this study. For a more detailed description of the model and the numerical methods used to solve it, the reader is referred to [13]. An in-depth discussion of a slightly different model, which is also of the Aker type [7], can be found in [14]. Both models were recently used to study the high capillary number regime [16].

The model describes flow of two incompressible and immiscible fluids (w and n) in a porous medium. The porous medium is represented by a network consisting of N nodes that are connected by M links. The nodes are each given an index $i \in [0, \dots, N - 1]$. The links are identified by the two nodes ij that they connect. An example pore network is shown in Figure 2. The nodes have no volume, and the pore space volume is thus assigned to the links. It is assumed that each fluid fills the entire link cross sections. The location of a fluid-fluid interface can therefore be described by a single number which gives its position in the link. For each link, the vector \mathbf{z}_{ij} contains the positions of the fluid interfaces in that link.

The flow in the links is treated in a one-dimensional fashion, averaged over the link cross sections. We consider flows in relatively small cross sections only and therefore neglect any effects of fluid inertia. The volumetric flow rate from node j to node i through the link connecting the two nodes is then given by,

$$q_{ij} = -\lambda_{ij}(\mathbf{z}_{ij}) \{p_i - p_j - c_{ij}(\mathbf{z}_{ij})\}. \quad (6)$$

Herein, p_i is the pressure in node i , λ_{ij} is the link's mobility and c_{ij} is the net pressure difference across the link due to its fluid interfaces. Both λ_{ij} and c_{ij} depend on the interface positions \mathbf{z}_{ij} . For two nodes i and j not connected by a link, $q_{ij} = 0$. Applying mass conservation at each node i yields,

$$\sum_j q_{ij} = 0. \quad (7)$$

The cross sectional area of link ij is a_{ij} . The interface positions \mathbf{z}_{ij} therefore evolve in time according to the advection equation,

$$\frac{d}{dt} \mathbf{z}_{ij} = \frac{q_{ij}}{a_{ij}}, \quad (8)$$

when sufficiently far away from the nodes. Close to the nodes, they are subject to additional models that account for interface interactions in the nodes. This is described in [13].

3.1. Link mobility model

The link mobility depends on link geometry and fluid viscosities. We assume cylindrical links when computing the mobilities and thus

$$\lambda_{ij}(\mathbf{z}_{ij}) = \frac{\pi r_{ij}^4}{8L_{ij}\mu_{ij}(\mathbf{z}_{ij})}. \quad (9)$$

Here, L_{ij} is the link length, r_{ij} is the link radius and $\mu_{ij}(\mathbf{z}_{ij})$ is the volume-weighted average of the fluid viscosities μ_w and μ_n .

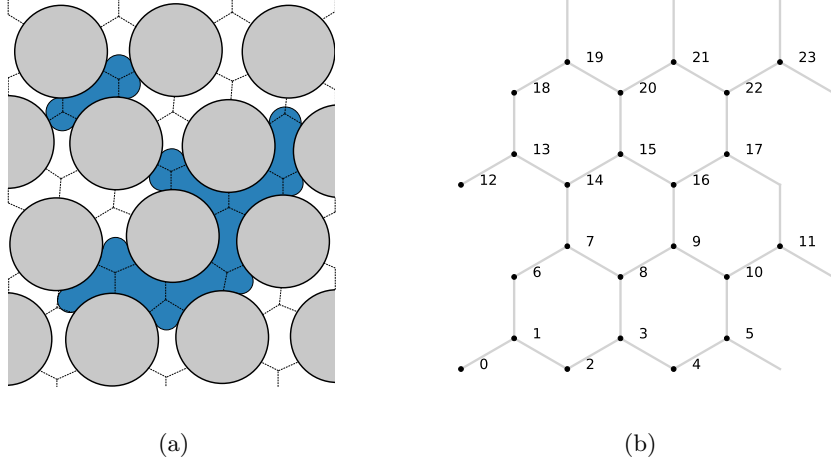


Figure 2: Illustration of (a) wetting (white) and non-wetting fluid (blue) in a physical pore network and (b) the representation of this network in the model. The dashed lines in (a) indicate sections of the pore space volume that are each represented by one link in (b). The intersection points of the dashed lines in (a) show the node locations in the model representation (b). Figures (a) and (b) are reproduced from [13].

3.2. Interfacial pressure discontinuity model

There may be zero, one or more interfaces in each link. Their positions along the link are contained in \mathbf{z}_{ij} . Each element in \mathbf{z}_{ij} is thus between 0 and L_{ij} . The symbol c_{ij} denotes the sum of the interfacial pressure discontinuities in link ij . We assume that the links are much wider near the ends than in the middle and that the pressure discontinuities become negligibly small for interfaces near the ends. The pressure discontinuities are therefore modeled by

$$c_{ij}(\mathbf{z}_{ij}) = \frac{2\sigma_{wn}}{r_{ij}} \sum_{z \in \mathbf{z}_{ij}} (\pm 1) \{1 - \cos(2\pi\chi(z))\}. \quad (10)$$

Herein, σ_{wn} is the interfacial tension and

$$\chi(z) = \begin{cases} 0, & \text{if } z < \beta r_{ij}, \\ \frac{z - \beta r_{ij}}{L_{ij} - 2\beta r_{ij}}, & \text{if } \beta r_{ij} < z < L_{ij} - \beta r_{ij}, \\ 1, & \text{if } z > L_{ij} - \beta r_{ij}. \end{cases} \quad (11)$$

The effect of the χ -function is to introduce zones of length βr_{ij} at each end of the links where the pressure discontinuity of any interface is zero.

3.3. Boundary conditions

In this study, we will run steady-state simulations in a network that can be laid out in two dimensions, as illustrated in Figure 2b. The network is periodic both in the flow direction and in the transverse direction. A pressure difference

of Δp will be applied across the periodic boundary in the flow direction, or a total flow rate Q will be prescribed, as described in [13]. The length of the network in the flow direction is denoted Δx and the average pressure gradient in the network is thus $\Delta p/\Delta x$.

3.4. Numerical solution method

Inserting (6) into (7) gives a system of equations for the unknown node pressures. The exact form of this system depends on the numerical method to be used. Here, we will use the Forward Euler method, where the length of time step n is set according to the criterions derived in [13],

$$\Delta t^{(n)} = \min \left(\Delta t_c^{(n)}, \Delta t_a^{(n)} \right). \quad (12)$$

Herein,

$$\Delta t_a^{(n)} = C_a \min_{ij} \left(\frac{a_{ij} L_{ij}}{q_{ij}^{(n)}} \right), \quad (13)$$

$$\Delta t_c^{(n)} = C_c \min_{ij} \left(\frac{2a_{ij}}{\lambda_{ij}^{(n)} \left| \sum_{z \in \mathbf{z}_{ij}^{(n)}} \frac{\partial c_{ij}}{\partial z} \right|} \right), \quad (14)$$

and the parameters C_a and C_c are set to 0.1 and 0.9, respectively, which together ensure numerical stability. Once the system is solved and the node pressures are obtained, the link flow rates can be calculated from (6) and the fluid interfaces moved according to (8). Further details can be found in [13].

3.5. Computation of average quantities from network simulations

The porous medium we consider is a network of links, and the total volume of the links is the pore volume V_p . The network is embedded in a three dimensional block of solid material with thickness Δx in the flow direction and cross sectional area A . The volume V of the porous block and its porosity φ are then easily calculated by (1) and (2), respectively.

The saturation S_w may be computed at any time during the simulation, by adding up the fluid volumes for all links. However, since we here use periodic boundary conditions, S_w is a constant in each simulation. So is $S_n = 1 - S_w$.

In the case of constant applied pressure gradient $\Delta p/\Delta x$, the quantities that we need to compute from the actual simulations are Q , Q_w and Q_n . These are time-averages of fluctuating quantities. The model is stepped forward in time as described in the previous section. We calculate the time-average Q by summing over the total flow rates $Q^{(n)}$ at each time step n (after steady-state has been reached),

$$Q = \frac{\sum_n Q^{(n)} \Delta t^{(n)}}{\sum_n \Delta t^{(n)}}. \quad (15)$$

The time-averaged quantities Q_w and Q_n is calculated from $Q_w^{(n)}$ and $Q_n^{(n)}$ in an analogous manner.

The instantaneous flow rate $Q^{(n)}$ can be computed by constructing a plane cutting through the network, transverse to the flow direction, and adding together the flow rates $q_{ij}^{(n)}$ of all links intersecting the plane. We denote the set of intersecting links by B and add up,

$$Q^{(n)} = \sum_{ij \in B} q_{ij}^{(n)}. \quad (16)$$

Since the fluids are incompressible, it does not matter where this cut is made.

The instantaneous flow rate $Q_w^{(n)}$ is computed by making several cuts, denote the set of cuts by C , and computing the sum

$$Q_w^{(n)} = \frac{1}{|C|} \sum_{B \in C} \sum_{ij \in B} s_{ij}^{(n)} q_{ij}^{(n)}. \quad (17)$$

Herein, $|C|$ denotes the number of elements in C , i.e. the number of cuts, and $s_{ij}^{(n)}$ is the volume fraction of wetting fluid in the volume of fluid that flowed past the middle of link ij during time step n . $Q_n^{(n)}$ is computed in an analogous manner. Having computed the time-averages Q , Q_w and Q_n we may obtain the time-averaged flow velocity, mobility, fractional flow and relative permeabilities.

If Q is fixed instead of $\Delta p / \Delta x$, the time-averaged value of the pressure gradient is computed by

$$\frac{\Delta p}{\Delta x} = \frac{\sum_n \Delta p^{(n)} \Delta t^{(n)}}{\Delta x \sum_n \Delta t^{(n)}}, \quad (18)$$

where $\Delta p^{(n)}$ is the pressure difference across the network during time step n .

Using average quantities calculated as described above, the capillary number is computed according to,

$$\text{Ca} = \frac{\bar{\mu} |Q|}{\varphi A \sigma_{wn}}, \quad (19)$$

where the average viscosity is defined as,

$$\bar{\mu} = S_w \mu_w + S_n \mu_n. \quad (20)$$

3.6. Dimensional analysis

As can be surmised from the description above, the network and five numbers are given as input to steady-state simulations. In the case of constant pressure-difference boundary conditions, the five numbers are the fluid viscosities μ_w and μ_n , the fluid-fluid interfacial tension σ_{wn} , the pressure gradient $\Delta p / \Delta x$ and the saturation S_w . Any change in the steady-state averages is the response of the model to variations in these inputs. If we consider the network topology and aspect ratios fixed, and only allow for a linear scaling of the network size, any

variations in the network can be described by a single length scale. We here choose the average pore radius \bar{r} .

By the Buckingham π theorem [18], the total of six dimensional input variables can be reduced to three dimensionless variables. This means that any combination of the six inputs that give the same three dimensionless variables are similar and differ only in scale. Any dimensionless output from the model is therefore the same for the same set of dimensionless input variables. One choice of dimensionless variables is

$$S_w, \quad (21)$$

$$M = \frac{\mu_n}{\mu_w}, \quad (22)$$

$$\Pi = \left| \frac{\Delta p}{\Delta x} \right| \frac{\bar{r}^2}{2\sigma_{wn}}, \quad (23)$$

where M is the viscosity ratio. The variable Π is a dimensionless pressure gradient. It represents the ratio of the average pressure drop over a length \bar{r} to the Young–Laplace pressure difference over an interface in a pore of radius \bar{r} . In particular, when $\Pi = 1$, we have

$$\left| \frac{\Delta p}{\Delta x} \right| \bar{r} = \frac{2\sigma_{wn}}{\bar{r}}, \quad (24)$$

and the average pressure drop over the length \bar{r} is equal to the typical Young–Laplace pressure difference.

Since it relates the average pressure drop to the capillary forces, Π may be expected to play a similar role as the capillary number. This should be true at least when capillary numbers are high and the average pressure drop is dominated by viscous contributions. However, Π is perhaps more closely related to the ganglion mobilization number. This was defined by Avraam and Payatakes [6] as the ratio between the driving force exerted on a ganglion and its resistance to motion resulting from capillary forces.

4. Simulations

Steady-state simulations were performed using the pore network model described in Section 3. All simulations were run on 72×48 hexagonal networks, similar to that shown in Figure 2b. These networks consisted of 3456 nodes and 5184 links. All links had the same length L and link radii were uniformly distributed between $0.1L$ and $0.4L$. In total, 6048 simulations were run with input parameters in the ranges given in Table 1. For each of the 288 combinations of the input parameters, 21 values of S_w were used, evenly spaced on the interval $[0, 1]$. Time-averaged quantities were calculated from simulation results as described in Section 3.5. The averaging time corresponded to 10 pore volumes of flow.

Table 1: Range of input parameters used in the steady-state pore network model simulations. For each combination of the input parameters, 21 values of S_w , evenly spaced on the interval $[0, 1]$, were used. The corresponding ranges of the dimensionless variables M , Π and Ca are also given (below the horizontal line).

Quantity	Minimum value	Maximum value	Unit
μ_w	$5.0 \cdot 10^{-4}$	$1.0 \cdot 10^{-2}$	Pa s
μ_n	$5.0 \cdot 10^{-4}$	$1.0 \cdot 10^{-2}$	Pa s
σ_{wn}	$2.0 \cdot 10^{-2}$	$3.0 \cdot 10^{-2}$	N m ⁻¹
$-\Delta p/\Delta x$	$3.9 \cdot 10^3$	$8.0 \cdot 10^5$	Pa m ⁻¹
\bar{r}	$2.5 \cdot 10^{-4}$	$7.8 \cdot 10^{-4}$	m
M	$5.0 \cdot 10^{-2}$	$2.0 \cdot 10^1$	-
Π	$6.1 \cdot 10^{-3}$	$8.1 \cdot 10^1$	-
Ca	$4.0 \cdot 10^{-4}$	$6.1 \cdot 10^{-1}$	-

5. Results

In this section, we present and discuss the simulation results. We look first at relative permeabilities (Section 5.1), then residual saturations (Section 5.2) average flow velocities and mobilities (Section 5.3) and, finally, fractional flows (Section 5.4).

5.1. Relative permeabilities

Relative permeabilities κ_w^r and κ_n^r are perhaps the most extensively studied properties in two-phase flow in porous media, and the most obvious dimensionless numbers to calculate from the pore network model. They relate the flow rates of each phase to the pressure drop through

$$\frac{Q_w}{A} = -\frac{\kappa_w^r \kappa}{\mu_w} \frac{\Delta p}{\Delta x}, \quad (25)$$

$$\frac{Q_n}{A} = -\frac{\kappa_n^r \kappa}{\mu_n} \frac{\Delta p}{\Delta x}, \quad (26)$$

where κ is the absolute permeability.

Computed relative permeabilities for a subset of the simulations are plotted in Figure 3, against saturation S_w and the non-dimensional pressure gradient Π . Specifically, Figure 3a, Figure 3b and Figure 3c show relative permeabilities for the wetting phase and viscosity ratios M of 1, 0.25 and 4, respectively. Relative permeabilities for the non-wetting phase and a viscosity ratio of 4 is shown in Figure 3d.

In all of these figures, i.e. for each value of M , the data fall on a single well-defined surface. This shows that the relative permeabilities are indeed determined by the three dimensionless variables S_w , M and Π , in agreement with the dimensional analysis in Section 3.6. Bardon and Longeron [19] mention that gravity (Bond number), wettability (contact angle) and inertia (Reynolds

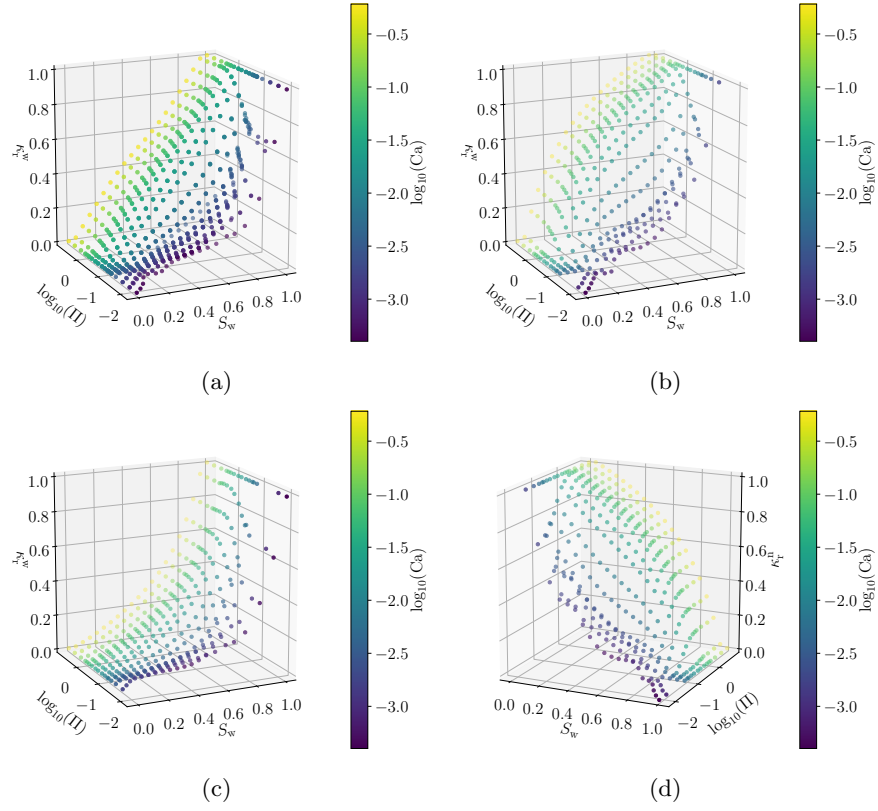


Figure 3: Relative permeabilities for the wetting phase for (a) $M = 1$, (b) $M = 0.25$ and (c) $M = 4$. Relative permeabilities for the non-wetting phase and $M = 4$ are shown in (d).

number) could also affect the relative permeabilities. These effects are not considered in the simulations run here, though gravity could be included in the model with relative ease.

When measuring relative permeabilities [11, 12] and when using relative permeability models to do continuum-scale calculations, it is often only their dependence on S_w which is considered. It is, however, well-established that variation with M and Ca cannot, in general, be neglected [6, 19]. Here, the calculated relative permeabilities are strongly dependent on Π , and they increase with increasing Π . In Figure 3, the color scheme shows that there is a strong correlation between Π and the capillary number, where high values of Π are also associated with high values of Ca . Thus, the results are consistent with those of Bardon and Longeron [19] and Avraam and Payatakes [6], who find that relative permeabilities increase with capillary number. This dependence seems to disappear, however, as $\Pi \rightarrow \infty$. For the viscosity ratios considered here, the dependence disappears at $\Pi \sim 1$. At this Π -value, the average pressure drop over the length \bar{r} is equal to the typical Young–Laplace interfacial pressure difference, as discussed in Section 3.6. The fact that the relative permeabilities become independent of the pressure gradient as capillary numbers increase is consistent with the existence of the high- Ca limit studied by Sinha et al. [16].

According to [4, 6, 19], relative permeabilities approach straight lines, i.e. $\kappa_w^r = S_w$ and $\kappa_n^r = 1 - S_w$, at high capillary numbers. In the equal-viscosity pore network simulations by Knudsen et al. [8], this was found to be the case. Here, however, we find straight lines only for $M \sim 1$. When M is different from unity, relative permeabilities converge to non-linear functions of S_w (and M) in the high- Ca limit.

One of the assumptions in the relative permeability framework is that the two fluids flow in decoupled flow channels [4]. When this is true, it is reasonable that the permeability of each fluid should be proportional to the cross sectional area of the porous medium available to it, i.e. proportional to the saturation, when capillary numbers are high. Such decoupled flow channels are not observed here. Instead, the fluids exhibit a large degree of mixing at high capillary numbers. This was observed also by Sinha et al. [16], both in pore network model and lattice-Boltzmann simulations. Disconnected non-wetting droplets were also observed at high capillary numbers in the experiments by Avraam and Payatakes [6], and were found to contribute significantly to the total flow rate, although connected pathways were also present. Our interpretation is therefore that the relative permeabilities may deviate from straight lines at high capillary numbers when the fluids mix instead of forming decoupled flow channels. The effect of this on total mobility and fractional flow is discussed further in Section 5.3 and Section 5.4, respectively.

From Figure 3, it is evident that the relative permeabilities follow a non-linear curve not unlike those produced by the classical Corey-type correlations for the lowest capillary numbers. When working with such correlations, it is typically assumed that there exists a low-capillary number limit below which relative permeabilities become independent of flow rate, and the correlations are valid (for the fluids used in the measurements). Ramstad et al. [4] mentions

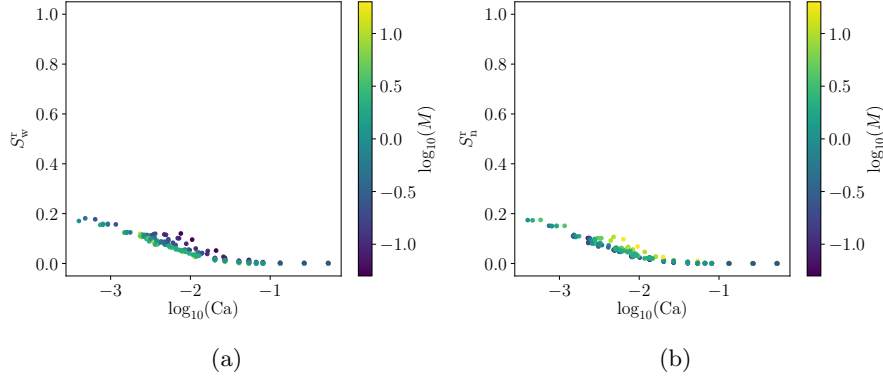


Figure 4: Residual saturations for (a) the wetting fluid and (b) the non-wetting fluid.

that viscous forces start to influence the fluid transport at capillary numbers around 10^{-5} . This is consistent with the findings here, which are that relative permeabilities have a dependence on Π down to the lowest capillary numbers considered of approximately 10^{-4} . We emphasize that the definition of capillary number used here differs from that used in [4], since it includes the porosity. Adoption of the definition from [4] would reduce all capillary numbers reported here by approximately half an order of magnitude.

Avraam and Payatakes [6] find from their experiments that both relative permeabilities increase with M . This is not the case here, at least not at high capillary numbers. They attribute this to effect to the existence of films of the wetting fluid, which are not included in our model.

5.2. Residual saturations

For both the wetting and non-wetting fluids, there are regions in Figure 3 where the relative permeabilities are zero. This was seen by Knudsen et al. [8] also, for $M = 1$. These regions correspond to irreducible/residual saturations, two other ubiquitous dimensionless quantities in two-phase porous media flow. The residual saturations are often defined as the saturation of one fluid that remains after flooding with the other. This property, defined in this way, is somewhat difficult to measure using the type of steady-state pore network model simulations performed here. Therefore, we have chosen to define the residual saturation of the wetting fluid as the saturation where the wetting fluid fractional flow falls below 10^{-4} . The residual non-wetting saturation is defined in an analogous manner. The value of this threshold is somewhat arbitrary, but it allows for a qualitative discussion.

Computed residual wetting and non-wetting saturations are shown in Figure 4. Residual saturations increase as capillary numbers are reduced, in accordance with findings of Ramstad et al. [4] and Bardon and Longeron [19]. Furthermore, they reach zero at at capillary numbers around 0.1. This means

that it is possible to flush out all of one fluid through flooding with the other, provided that the flow rate is high enough.

Bardon and Longeron [19] also observed that residual saturations were insensitive to changes in M , and this is what we see here also. Wetting residual saturations are somewhat higher when the wetting fluid is more viscous and non-wetting residual saturations are a little higher when the non-wetting fluid is more viscous, but this effect appears small.

5.3. Average flow velocity and mobility

The average mobility m and the average flow velocity v are other important quantities. They are related through

$$v = -m \frac{\Delta p}{\Delta x}, \quad (27)$$

and are discussed together here for reasons that will become apparent below.

Sinha et al. [16] studied the high-Ca limit of two-phase porous media flow. They found that, at high capillary numbers, the average flow velocity followed a Darcy-type equation,

$$v_D = -m_D \frac{\Delta p}{\Delta x} = -\frac{\kappa}{\bar{\mu}\varphi} \frac{\Delta p}{\Delta x}, \quad (28)$$

with an effective viscosity

$$\bar{\mu}^\alpha = S_w \mu_w^\alpha + S_n \mu_n^\alpha. \quad (29)$$

The exponent α depended on the degree of mixing of the fluids, induced by the flow through the porous medium, and was 0.6 for the porous medium studied here.

The value 0.6 of the exponent α is a direct result of the departure of the relative permeabilities from straight lines at high capillary numbers. If the relative permeabilities were straight lines, we would have $\alpha = -1$ and v_D/v_0 could then be expressed as a linear function of S_w ,

$$v_D/v_0|_{\alpha=-1} = 1 + S_w(M - 1), \quad (30)$$

where v_0 is the flow velocity in the single-phase case where $S_w = 0$. Instead, with $\alpha = 0.6$, v_D/v_0 is a non-linear function of S_w .

The existence of this high-Ca limit motivates the study of the average flow velocity and the average mobility, relative to their limit values. Dividing (27) by (28) gives

$$v/v_D = m/m_D. \quad (31)$$

The two quantities v/v_D and m/m_D are thus identical. Moreover, they are dimensionless and may be expected to vary, roughly, between 0 and 1. In particular, they should be 1 in the two single-phase cases, $S_w = 1$ and $S_n = 1$, and in the high-Ca limit.

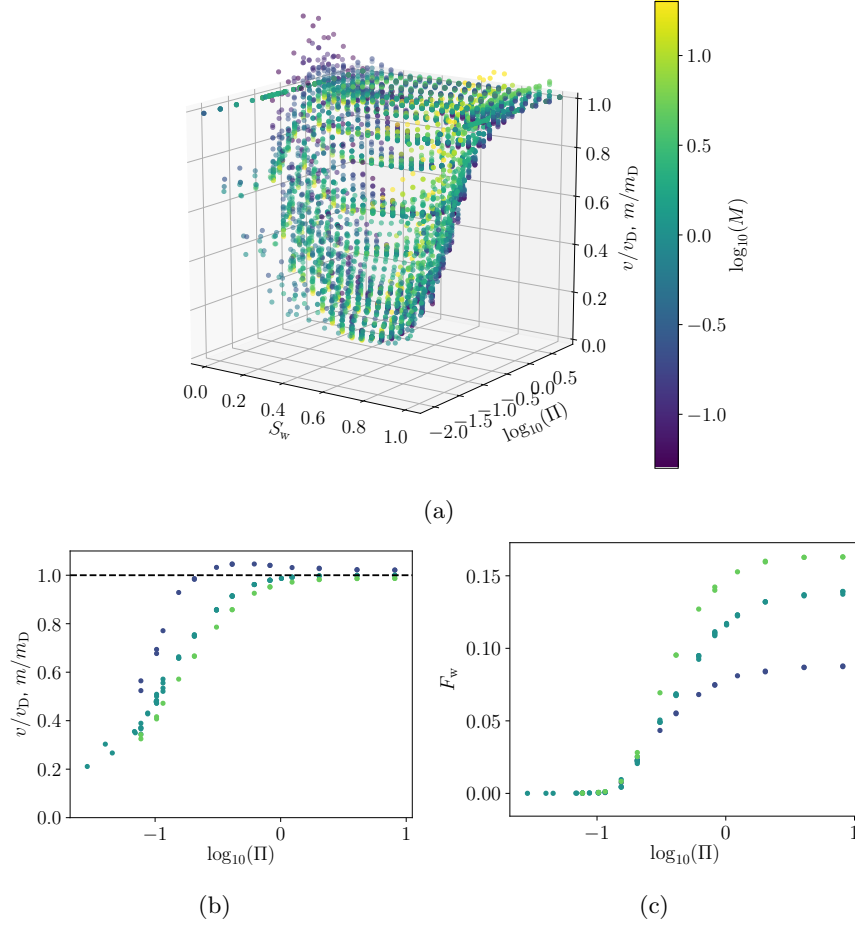


Figure 5: (a) Calculated values of v/v_D for all simulations performed. (b) Calculated values of v/v_D for a subset of the simulations in (a) with $S_w = 0.15$ and viscosity ratios of 0.2, 1 and 5. (c) Fractional flow for the same set of simulations as in (b).

Figure 5a shows v/v_D for all simulations run, plotted against S_w and Π . As expected, all data points collapse to 1 in both single-phase cases. Furthermore, each value of M corresponds to a single well-defined v/v_D -surface, in accordance with the dimensional analysis. From the figure, however, it is evident that these surfaces are not overly sensitive to M , at least not for S_w around 0.5. Each constant- M surface reaches values close to 1 at the highest values of Π , in agreement with the findings of Sinha et al. [16] for the high-Ca limit.

Interestingly, there are some values of v/v_D that are larger than 1. These occur for the more disparate viscosity ratios, at saturations where the more viscous fluid is in minority. Figure 5b shows v/v_D plotted against Π , for $S_w = 0.15$ and three different viscosity ratios, 0.2, 1 and 5. The data points with $M = 1$ converge to 1, the limit value, from below and relatively fast as Π increases. The data points with $M = 5$ also approach 1 from below, but slower. For the lower viscosity ratio $M = 0.2$, on the other hand, v/v_D increases fast, overshoots and then approaches 1 from above.

In Figure 5c is shown the fractional flow for the same data points as in Figure 5b. For the data points with $M = 1$, convergence of v/v_D to the limit value occurs as the fractional flow approaches its limit value. The same is true for $M = 0.2$ and $M = 0.5$, although convergence is not yet complete for the largest Π -values considered.

In terms of mobility ratios m/m_D these observations may be understood as follows. At low pressure gradients, all wetting fluid is stuck, in the sense that $F_w = 0$, and the non-wetting fluid flows around it (see Figure 5c). As the pressure gradient is increased, some of the wetting fluid is mobilized and F_w increases above zero. This results in more active flow paths for both fluids and a sharp increase in the average mobility for all three viscosity ratios.

For $M = 0.2$, average mobility reaches a maximum before all wetting fluid is mobilized, i.e. before F_w converges to its value in the high-Ca limit. This maximum is caused by the competition between two different effects. First, an increase in pressure gradient makes more flow paths available, increasing mobility. Second, F_w increases and the more viscous wetting fluid makes up a larger fraction of the flowing fluid. Thus the average viscosity of the flowing fluid increases, reducing the average mobility. Eventually, a point is reached where the latter effect becomes more important and a further increase in the pressure gradient reduces the average mobility.

For $M = 1$, there is no such competition to generate a maximum, as the wetting and non-wetting fluids are equally viscous and mobilization of the wetting fluid does not affect the average viscosity.

For $M = 5$, the two effects are again present. However, since the wetting fluid is now less viscous, they both lead to an increase in mobility with an increase in pressure gradient and we see no maximum.

The mobility ratios m/m_D for $M = 5$ lie below those for $M = 1$ and they converge slower to the high-Ca limit. A possible reason for this is that it requires a higher (non-dimensional) pressure gradient to converge the average viscosity, not changed in the case of $M = 1$, to its high-Ca limit than to mobilize all flow paths in the porous medium.

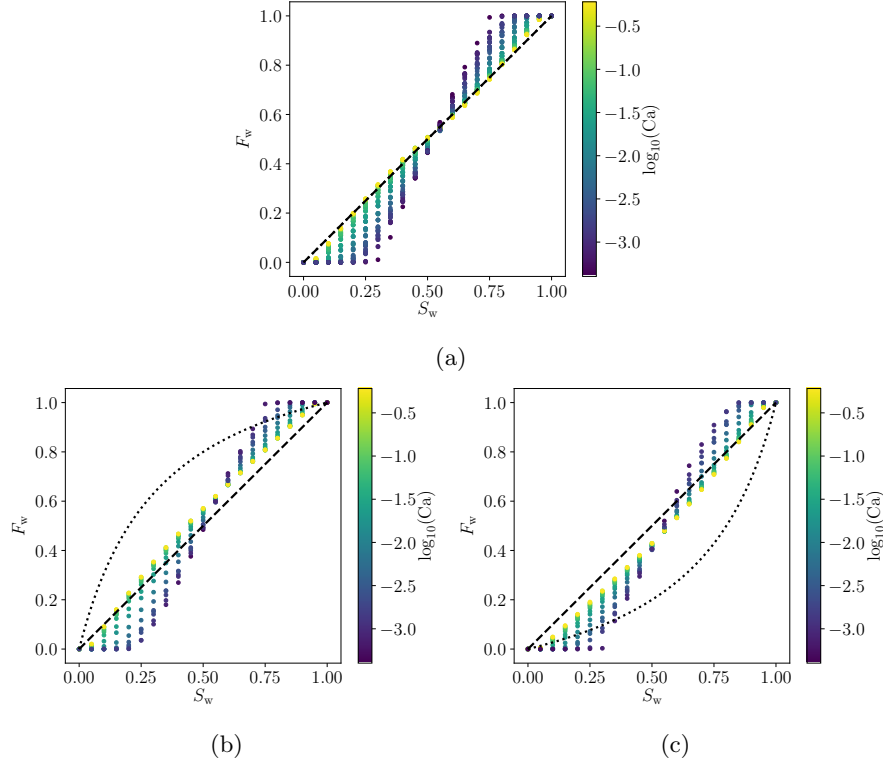


Figure 6: Fractional flow data for (a) $M = 1$, (b) $M = 4$ and (c) $M = 0.25$. The dashed lines represent $F_w = S_w$ and the dotted lines represent the fractional flow obtained if the relative permeabilities were $\kappa_w^r = S_w$ and $\kappa_n^r = 1 - S_w$.

5.4. Fractional flow

The fractional flow for a subset of the performed simulations are shown in Figure 6, for viscosity ratios 1, 4, and 0.25.

The data in Figure 6a for $M = 1$ are in qualitative agreement with those from Knudsen et al. [8]. They find $F_w \sim S_w$ at high capillary numbers, i.e. in the viscosity-dominated regime. The deviation from the diagonal line representing $F_w = S_w$ increases as the capillary number is reduced. Furthermore, curves for a specific capillary number are asymmetric w.r.t. $S_w = 0.5$ and cross the diagonal line at $S_w > 0.5$, meaning that more of the curve lies below the diagonal than above it. This observation was explained by Knudsen et al. [8] by the propensity for the wetting fluid to occupy narrower pores where flow rate is lower.

By comparing Figure 6b and Figure 6c we may deduce some of the impact of the viscosity ratio on the fractional flow. At high capillary numbers, $F_w > S_w$ when $M > 1$, i.e. when the wetting fluid is less viscous. Conversely, $F_w < S_w$ when $M < 1$ and the wetting fluid is more viscous. The latter was observed also by Avraam and Payatakes [6], at low viscosity ratios and high capillary number,

the fractional flow curves tended to curve upwards.

The dotted lines in Figure 6b and Figure 6c represent the fractional flows obtained if the relative permeabilities were $\kappa_w^r = S_w$ and $\kappa_n^r = 1 - S_w$, i.e. if the fluids followed separate flow channels. We therefore conclude that mixing of the fluids cause the flow rates Q_w and Q_n to be closer to each other and the fractional flow curves to lie closer to the diagonal than they would if the fluids flowed in decoupled flow channels.

At lower capillary numbers, the fractional flow curves obtain the classical S-shape, as in the case for $M = 1$. Also, as is intuitive and was observed by Avraam and Payatakes [6], fractional flow for a given saturation and capillary number increases with viscosity ratio.

6. Conclusion

We have performed more than 6000 steady-state simulations with a dynamic pore network model of the Aker type [7], corresponding to a large span in viscosity ratios and capillary numbers. From these simulations, dimensionless quantities such as relative permeabilities, residual saturations, mobility ratios and fractional flows were computed and discussed. By a dimensional analysis of the model, all dimensionless output was found to be functions of the saturation S_w , the viscosity ratio M and the dimensionless pressure gradient Π . Effects of wettability, gravity and inertia were not considered. These effects may add additional dimensionless variables whose impact could be studied in future work.

Calculated relative permeabilities and residual saturations showed many of the same qualitative features observed in other experimental and modeling studies. In particular, the relative permeabilities increased with capillary numbers and converged to a limit, dependent on M and S_w , at high capillary numbers. However, while other studies find that relative permeabilities converge to straight lines at high capillary numbers we found that this is not the case when $M \neq 1$. Our conclusion was that departure from straight lines occurs when fluids mix rather than form decoupled flow channels when capillary numbers are high. Such mixing behavior has been observed in previously in pore network and lattice-Boltzmann simulations [16] and, to some extent, in experiments [6]. However, it would be very interesting to see if experimental studies specifically designed to induce mixing and measure steady-state properties at high capillary numbers would produce relative permeability curves that are non-linear in S_w .

Another consequence of the mixing was that computed fractional flow curves, plotted against saturation, lay closer to the diagonal than expected from assuming decoupled flow channels. At lower capillary numbers, fractional flow curves obtained a classical S-shape.

Ratios of average mobility to their high-capillary number limit values were also considered. These ratios varied, roughly, between 0 and 1, but values larger than 1 were also observed. For a given saturation and viscosity ratio, the mobilities were not always monotonically increasing with the pressure gradient. While increasing the pressure gradient mobilized more fluid and activates more

flow paths, when the mobilized fluid is more viscous, a reduction in average mobility may occur instead.

Acknowledgments

The authors would like to thank Signe Kjelstrup and Santanu Sinha for discussions and encouragement. This work was partly supported by the Research Council of Norway through its Centres of Excellence funding scheme, project number 262644.

References

- [1] A. Q. Raeini, M. J. Blunt, and B. Bijeljic. Modelling two-phase flow in porous media at the pore scale using the volume-of-fluid method. *Journal of Computational Physics*, 231(17):5653–5668, 2012. doi: 10.1016/j.jcp.2012.04.011.
- [2] E. Jettestuen, J. O. Helland, and M. Prodanović. A level set method for simulating capillary-controlled displacements at the pore scale with nonzero contact angles. *Water Resources Research*, 49(8):4645–4661, 2013. doi: 10.1002/wrcr.20334.
- [3] M. Aa. Gjennestad and S. T. Munkejord. Modelling of heat transport in two-phase flow and of mass transfer between phases using the level-set method. *Energy Procedia*, 64:53–62, 2015. doi: 10.1016/j.egypro.2015.01.008.
- [4] T. Ramstad, N. Idowu, C. Nardi, and P.-E. Øren. Relative permeability calculations from two-phase flow simulations directly on digital images of porous rocks. *Transport in Porous Media*, 94:487–504, 2012. doi: 10.1007/s11242-011-9877-8.
- [5] B. Zhao, C. W. MacMinn, B. K. Primkulov, Y. Chen, A. J. Valocchi, J. Zhao, Q. Kang, K. Bruning, J. E. McClure, C. T. Miller, A. Fakhari, D. Bolster, T. Hiller, M. Brinkmann, L. Cueto-Felgueroso, D. A. Cogswell, R. Verma, M. Prodanovi, J. Maes, S. Geiger, M. Vassvik, A. Hansen, E. Segre, R. Holtzman, Z. Yang, C. Yuan, B. Chareyre, and R. Juanes. Comprehensive comparison of pore-scale models for multiphase flow in porous media. *Proceedings of the National Academy of Sciences*, 116(28):13799–13806, 2019. doi: 10.1073/pnas.1901619116.
- [6] D. Avraam and A. Payatakes. Flow regimes and relative permeabilities during steady-state two-phase flow in porous media. *Journal of Fluid Mechanics*, 293:207–236, 1995. doi: 10.1017/S0022112095001698.
- [7] E. Aker, K. J. Måløy, A. Hansen, and G. G. Batrouni. A two-dimensional network simulator for two-phase flow in porous media. *Transport in porous media*, 32(2):163–186, 1998. doi: 10.1023/A:1006510106194.

- [8] H. A. Knudsen, E. Aker, and A. Hansen. Bulk flow regimes and fractional flow in 2D porous media by numerical simulations. *Transport in Porous Media*, 47(1):99–121, 2002. doi: 10.1023/A:1015039503551.
- [9] H. A. Knudsen and A. Hansen. Relation between pressure and fractional flow in two-phase flow in porous media. *Physical Review E*, 65(5):056310, 2002. doi: 10.1103/PhysRevE.65.056310.
- [10] T. Ramstad and A. Hansen. Cluster evolution in steady-state two-phase flow in porous media. *Physical review E*, 73(2):026306, 2006. doi: 10.1103/PhysRevE.73.026306.
- [11] M. J. Oak, L. E. Baker, and D. C. Thomas. Three-phase relative permeability of Berea sandstone. *Journal of Petroleum Technology*, 42(08):1054–1061, 1990. doi: 10.2118/17370-PA.
- [12] B. Bennion and S. Bachu. Relative permeability characteristics for supercritical CO₂ displacing water in a variety of potential sequestration zones. In *SPE Annual Technical Conference and Exhibition*. Society of Petroleum Engineers, 2005. doi: 10.2118/95547-MS.
- [13] M. Aa. Gjennestad, M. Vassvik, S. Kjelstrup, and A. Hansen. Stable and efficient time integration at low capillary numbers of a dynamic pore network model for immiscible two-phase flow in porous media. *Frontiers in Physics*, 6, 2018. doi: 10.3389/fphy.2018.00056.
- [14] S. Sinha, M. Aa. Gjennestad, M. Vassvik, and A. Hansen. A dynamic network simulator for immiscible two-phase flow in porous media. *Transport in Porous Media*, 2019. URL <https://arxiv.org/abs/1907.12842>. Under review.
- [15] G. Tørå, P.-E. Øren, and A. Hansen. A dynamic network model for two-phase flow in porous media. *Transport in porous media*, 92(1):145–164, 2012. doi: 10.1007/s11242-011-9895-6.
- [16] S. Sinha, M. Aa. Gjennestad, M. Vassvik, M. Winkler, A. Hansen, and E. G. Flekkøy. Rheology of high-capillary number flow in porous media. *Frontiers in Physics*, 7, 2019. doi: 10.3389/fphy.2019.00065.
- [17] A. Hansen, S. Sinha, D. Bedeaux, S. Kjelstrup, M. Aa. Gjennestad, and M. Vassvik. Relations between seepage velocities in immiscible, incompressible two-phase flow in porous media. *Transport in Porous Media*, 125:565–587, 2018. doi: 10.1007/s1124.
- [18] R. Rayleigh. On the question of the stability of the flow of fluids. *The London, Edinburgh, and Dublin Philosophical Magazine and Journal of Science*, 34(206):59–70, 1892. doi: 10.1080/14786449208620167.
- [19] C. Bardon and D. G. Longeron. Influence of very low interfacial tensions on relative permeability. *Society of Petroleum Engineers Journal*, 20(05):391–401, 1980. doi: 10.2118/7609-PA.